INTERACTION BETWEEN WAVES AND HANGING HIGHLY FLEXIBLE KELP BLADES

Long-Huan Zhu[1], Kimberly Huguenard[2], and David Fredriksson[3]

The interaction between waves and flexible blades has drawn recent attention because of the capacity of nature-based infrastructure, such as aquatic vegetation and kelp, to attenuate waves. In this study, a new numerical model was developed to study the wave-blade interaction for both bottom-fixed and suspended blades. The dynamics of the blades simulated by a cable model were coupled with OpenFOAM®-based wave model IHFoam with the immersed boundary method. The results showed that the distribution of the blade-induced vortices was asymmetric with more vortices upstream for the single bottom-fixed blade while more vortices downstream for the single suspended blade. For both submerged and suspended canopies, the vortex distribution is also asymmetric. More vortices concentrate upstream for the submerged canopy. For a suspended canopy, more vortices concentrate upstream and below the bottom of the suspended canopy. Yet near the surface above the suspended canopy, more vortices concentrate downstream. Understanding the distribution of vortices is important for predicting the sediment transport and nutrient distribution.

INTRODUCTION

The wave attenuation capacity of vegetation has drawn recent attention due to its potential to serve as an ecological alternative to hardened coastal protection. Most previous studies focused on the effects of bottom aquatic plants such as seagrasses, wetlands, mangroves, and salt marshes. Only until recently have researchers considered the impacts of near-surface aquaculture structures such as kelp. The wave-attenuation capacity of a suspended canopy was investigated by Zhu and Zou (2017) using a three-layer analytical model without considering the flexibility of the blade, which overestimated wave decay. The results did showed that suspended canopies damped intermediate and deep-water waves more significantly than submerged canopies. Using a non-hydrostatic model called SWASH (Simulating WAves till SHore), Chen et al. (2018) investigated the effects of suspended and floating canopies on wave attenuation as well as wave-canopy induced currents. Their results showed that the analytical solution by Zhu and Zou (2017) was in good agreement with the numerical results for small wave height decay rate. For a larger wave height rate, the analytical solution by Zhu and Zou (2017) predicted a larger wave height decay.

Additional work by Alben et al. (2002) showed that interaction between waves and flexible blades needs to be considered since blade deformation reduces drag force resulting in a weaker wave attenuation capacity (Mullarney and Henderson, 2010). The wave-induced dynamics of a flexible bottom-fixed blade was investigated by Luhar and Nepf (2016) using experimental and numerical methods. Luhar et al. (2017) examined wave attenuation by flexible blades by representing compliance as a shortened effective length.

Building on this body of work, the objective of this paper was to develop a numerical model to study the wave-blade interaction for both bottom-fixed and suspended blades. The dynamics of the flexible blades were built as a cable model and coupled with the OpenFoam®-based wave model IHFoam applying the immersed boundary method. The coupled model was compared with experiments done by Luhar and Nepf (2016). The dynamic model was used to investigate wave-blade interactions by analyzing the distribution of vortices for both bottom-fixed and suspended blades as well as submerged and suspended canopies.

METHODOLOGY

Cable model for blade dynamics

The swaying nature of kelp blades can be simulated using a cable model (Howell, 1992; Trianrafyllou, 1994) since it incorporates large deformations, as shown in Fig 1. In this 2D model, the fixed global Cartesian reference frame (x, z) with the origin (O) at the bottom end of the blade is defined in Fig. 1(a), where x and z indicate the horizontal and vertical directions, respectively. To derive the governing equations representing the blade dynamics, a Lagrangian coordinate system $(\vec{t}, \vec{n})$ along the blade length is used, where $\vec{t}$ and $\vec{n}$ indicate the blade-parallel and blade-normal directions, respectively. In this model, the twisting motion of the blade neglected. The velocity of the blade segment ds is denoted as $\vec{u} = (u, v)$, where u and v are the components in the blade-parallel and blade-normal directions,

---

[1] Department of Civil and Environmental Engineering, University of Maine, Orono, ME, 04469-5711, USA.
  Corresponding author: longhuan.zhu@maine.edu
[2] Department of Civil and Environmental Engineering, University of Maine, Orono, ME, 04469-5711, USA.
[3] Department of Naval Architecture and Ocean Engineering, U.S. Naval Academy, Annapolis, MD, 21402, USA

respectively. The distance along the length of the blade (l) from the origin is s. The local bending angle of the blade relative to the vertical direction is ϕ, where $\phi = 0$ denotes an upright posture.
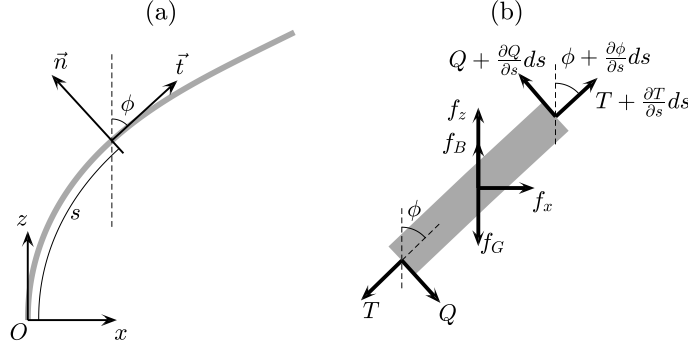
Figure 1. Schematic diagram for the coordinate systems and the free-body diagram. (a) Fixed global Cartesian reference frame (x, z) and the local Lagrangian coordinate system $(\vec{t}, \vec{n})$ along the blade length (s), where $\vec{t}$ and $\vec{n}$ indicate blade-parallel and blade-normal directions. The thin gray line denotes the flexible blade and the thin arrows denote axes. (b) A free-body diagram for one segment of the flexible blade ds used in the wave-vegetation model. The thick gray line denotes the blade segment ds with an angle ϕ with vertical axis and the thick arrows denote forces. The internal forces include the effective tension (T), shear (Q), and the external forces per unit blade length include the gravity (f_G), buoyancy (f_B), and hydrodynamic force $\vec{f} = (f_x, f_z)$.

The blade dynamics are governed by the equilibrium of the internal and external forces, as shown in Fig. 1(b). The internal forces include the effective tension (T) in the blade-parallel direction and shear (Q) in the blade-normal direction, respectively. The external forces per unit blade length consist of the buoyancy (f_B), gravity (f_G), and hydrodynamic forces $\vec{f} = (f_x, f_z)$. Based on the equilibrium of momentum, the govern equations are

$$\rho_v bd \left(\frac{\partial u}{\partial t} + v \frac{\partial \phi}{\partial t} \right) = Q \frac{\partial \phi}{\partial s} + \frac{\partial T}{\partial s} + (f_z - f_G) \cos \phi + f_x \sin \phi \qquad (1)$$

and

$$\rho_v bd \left(\frac{\partial v}{\partial t} - u \frac{\partial \phi}{\partial t} \right) = \frac{\partial Q}{\partial s} - T \frac{\partial \phi}{\partial s} + (f_z - f_G) \sin \phi - f_x \cos \phi, \qquad (2)$$

where ρ_v is the blade density, b is the blade width, and d is the blade thickness. The blade is assumed to be a linear material such that shear (Q) is proportional to curvature:

$$Q = EI \frac{\partial^2 \phi}{\partial s^2}, \qquad (3)$$

where I is the second area moment of the blade cross-section and E is the elastic modulus. To satisfy geometric continuity of the segments, the compatibility relations are applied such that

$$\frac{\partial u}{\partial s} + v \frac{\partial \phi}{\partial s} - \frac{1}{Ebd} \frac{\partial T}{\partial t} = 0, \qquad (4)$$

and

$$\frac{\partial v}{\partial s} - u \frac{\partial \phi}{\partial s} + \frac{\partial \phi}{\partial t} = 0. \qquad (5)$$

The boundary conditions for the fixed end are given by

$$u = 0, v = 0, \phi = 0 \qquad (6)$$

and for the free end:

$$T = 0, \frac{\partial \phi}{\partial s} = 0, \frac{\partial^2 \phi}{\partial s^2} = 0. \qquad (7)$$

For bottom-rooted vegetation, the bottom end of the blade is fixed and the top end is free. While for the hanging kelp blade, the bottom end of the blade is free and the top end is fixed.

OpenFOAM®-based wave model IHFoam

The interFoam solver incorporating the Volume of Fluid (VOF) method for multiphase flow built in OpenFOAM® is used to simulate the water surface waves. Following Higuera et al. (2013) and Chen et al. (2017), the governing equations for the fluid domain are given by

$$\nabla \cdot \vec{U} = 0, \tag{8}$$

$$\frac{\partial \rho \vec{U}}{\partial t} + \nabla \cdot \left(\rho \vec{U} \vec{U} \right) - \nabla \cdot \left(\mu_{eff} \nabla \vec{U} \right) = -\nabla p^* - \vec{g} \cdot \vec{X} \nabla \rho + \nabla \vec{U} \cdot \nabla \mu_{eff} - \vec{F}, \tag{9}$$

and

$$\frac{\partial \alpha}{\partial t} + \nabla \cdot \left(\vec{U} \alpha \right) + \nabla \cdot \left(\overrightarrow{U_C} \alpha (1 - \alpha) \right) = 0, \tag{10}$$

where $\vec{U}$ is the fluid velocity vector on the fluid domain with Euler mesh, ρ is the fluid density, p^* is the pseudo-dynamic pressure, $\vec{g}$ is the gravitational acceleration, $\vec{X}$ is the position vector, μ_{eff} is the effective dynamic viscosity, $\vec{F}$ is the blade-induced boundary forces spreading to the Euler mesh, and α is the quantity of water per unit of volume at each cell, $\left| \overrightarrow{U_C} \right| = \min \left[c_\alpha |\vec{U}|, \max(|\vec{U}|) \right]$, and c_α can be specified by user with default value of 1. The open-source package IHFoam, based on OpenFOAM (Higuera et al., 2013; Chen et al., 2017), was used to generate and absorb waves at the inlet and outlet boundaries.

Immersed boundary method for wave-blade interaction

The immersed boundary method (Peskin, 2002) is used to represent the coupling of waves and blades. According to the immersed boundary method, a no-slip boundary condition is applied at the interface between the fluid and structure by adding a force (source) term to the momentum equations in the fluid domain (Eq. 9). With this technique, the fluid mesh near the interface does not need to adapt to the shape of the structure. Therefore, the fluid mesh can be built as a structured Cartesian grid, increasing the computational efficiency and stability.

The explicit scheme for the weak coupling of the waves and blade dynamics is shown in Fig. 2. For
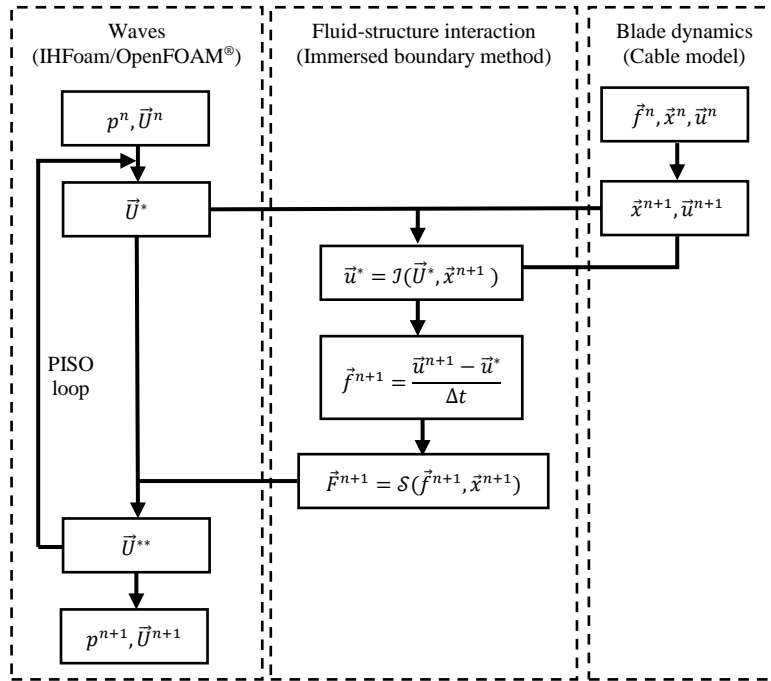
Figure 2. Flow chart of the explicit scheme for the weak coupling of waves and blade dynamics. The superscript n indicates the nth time step. For the computation in the fluid domain, p is the fluid pressure, $\vec{U}$ is the fluid velocity vector, and $\vec{F}$ is the boundary force spreading to the fluid domain with spreading operator S. According PISO algorithm, $\vec{U}^*$ is the first predictor of the fluid velocity vector and $\vec{U}^{**}$ is the second predictor of the fluid velocity vector. For the computation of blade dynamics, $\vec{x}$ is the blade position vector and $\vec{u}$ is the blade velocity vector, and $\vec{f}$ is the hydrodynamic force acting on the blade mesh. The interpolation of the fluid velocity on the blade mesh is $\vec{u}^*$ calculated with interpolation operator J.

weak coupling, the iteration of computation for the blade is not implemented. At the nth time step, the new velocity ($\vec{u}^{n+1}$) and position ($\vec{x}^{n+1}$) of the blade at $(n + 1)$th time step is obtained by Eq. 1 through Eq. 7 based on the cable model. Pressure-Implicit with Splitting of Operators (PISO) algorithm is used in the computation in the fluid domain with two predictor velocity vectors. The first predictor velocity

vector ($\vec{U}^*$) of the fluid domain is solved by OpenFOAM®. The interpolation of the first predictor velocity vector ($\vec{U}^*$, Euler mesh) on the blade position ($\vec{x}^n$, Lagrangian points) at n^{th} time step can be obtained using the interpolation operator ($\mathcal{I}$) and given by

$$\vec{u}^* = \mathcal{I}\left(\vec{U}^*, \vec{x}^{n+1}\right), \tag{11}$$

where the calculation for the interpolation operator ($\mathcal{I}$) is given by Constant et al. (2017) and Riahi et al. (2018). Then the force term at the Lagrangian points at $(n+1)^{\text{th}}$ time step can be obtained:

$$\vec{f}^{n+1} = \frac{\vec{u}^{n+1} - \vec{u}^*}{\Delta t}, \tag{12}$$

where the time step is Δt. Eq. 12 shows the no-slip condition at the interface between the fluid and the blade. The force term on Lagrangian points are spread to the enclosed Euler mesh in order to obtain the force term on Euler mesh, which is expressed as

$$\vec{F}^{n+1} = \mathcal{S}\left(\vec{f}^{n+1}, \vec{x}^{n+1}\right), \tag{13}$$

where the spreading operator ($\mathcal{S}$) is the inverse calculation of the interpolation operator. Implementing the force term in the fluid momentum equation yields the second predictor velocity field ($\vec{U}^{**}$). With this updated fluid velocity, the computation within the fluid domain returns back to the step of calculating the first predictor velocity vector again to continue the PISO loop until the fluid velocity reaches convergence. Finally, the pressure (p^{n+1}) and the velocity field ($\vec{U}^{n+1}$) of the fluid are obtained.

DATA COMPARISON

Since there is no published data for the interaction between waves and hanging flexible blades, the coupled model is compared with the results of experiments conducted by Luhar and Nepf (2016) for bottom-fixed blades. The experiments were performed in a 24 m × 38 cm × 60 cm wave flume with the experiment setup shown in Fig. 3. An 8 cm high acrylic box was installed in the middle of the flume to mount the load cell which was attached to the bottom of the blade to measure the horizontal force. The blade was fixed at 4 cm above the acrylic box by a holder. With the acrylic box, the effective depth of the tank was 30 cm. Waves with a period of 2 second waves with an amplitude of 4 cm were used during the experiments. The wave orbital velocity at 15 cm ahead of the blade is measured by with a PIV (particle image velocimetry) system. The length of the model blade was 20 cm, the width was 2 cm, and the thickness was 0.4 mm. The density of the blade was 950 kg/m³. The elastic modulus of the blade was 500 kPa.
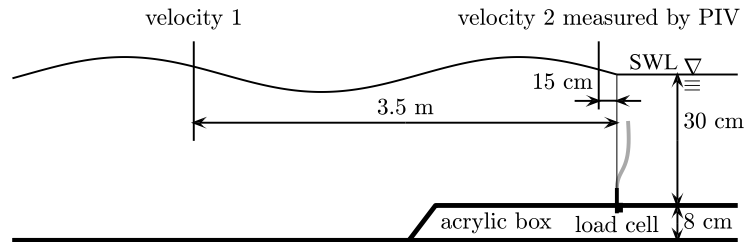
Figure 3. Schematic diagram for the experimental setup. The blade (gray line) is located on the top of the acrylic box. The still water line (SWL) is 38 cm above the bottom, which is also 30 cm above the acrylic box. The investigated wave orbital velocities at position 1 (3.5 m ahead the blade) and position 2 (15 cm ahead the blade) are 32 cm above the bottom. Velocity 2 was measured with a PIV (particle image velocimetry) system by Luhar and Nepft (2016. The waves are propagated from left to right.

The computational domain was created to be12 m long (3.68 wavelengths) and 0.53 m high. The smallest grid size was set at 0.002 m × 0.002 m for the mesh near the blade. The mesh size for the blade was also 0.002 m. The grid size was increased gradually to the edge of the computational domain and the number of cells is 370780.

Stokes Second Order wave theory was applied with $ka = 0.0771$ and $kh = 0.5786$, where k was the wave number, a was the wave amplitude, and h was the water depth. Once the simulations were complete, wave orbital velocities at two points were measured including: (1) 3.5 m ahead the blade and 32 cm above the bottom and (2) 15 cm ahead the blade and at the same level (shown in Fig.3). The comparison between the time series of the wave orbital velocities predicted by the coupled model and Stokes Second Order wave theory, as well as the measured data, are shown in Fig. 4. The predicted wave orbital velocity 3.5 m ahead the blade follows closely with the wave theory, except for a small

underestimation for the horizontal component at the wave trough, as shown in Fig. 4(a). For the wave orbital velocity near the blade (15 cm ahead), the underestimation of the horizontal component at wave trough increases slightly, while the predicted vertical component is smaller than the wave theory at the wave crest. The modeled horizontal component is in good agreement with the data. However, the predicted vertical component is larger than the measured data.
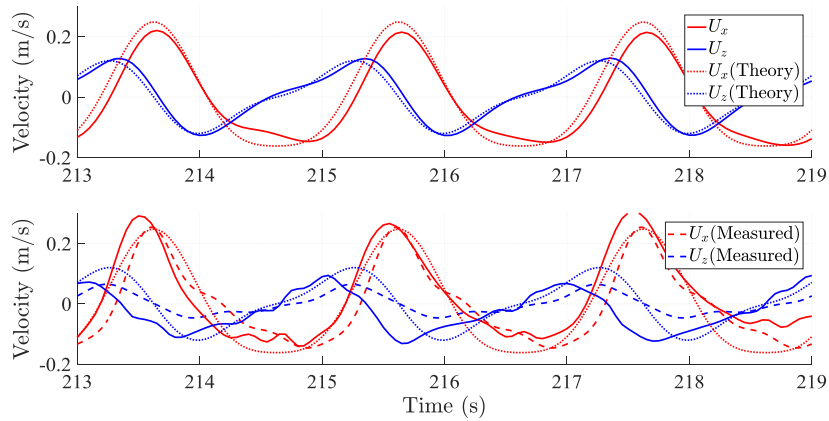
Figure 4. Wave orbital velocities at the points (a) 3.5 m ahead the blade and (b) 15 cm ahead the blade and 32 cm above the bottom without the acrylic box (see Fig. 3). The red lines denote the horizontal components while the blue lines denote the vertical components. The solid lines denote the predictions by the present model, the dotted lines denote the results based on Stokes II wave theory, and the dashed lines denote the measured data by Luhar and Nepf (2016) with PIV system.
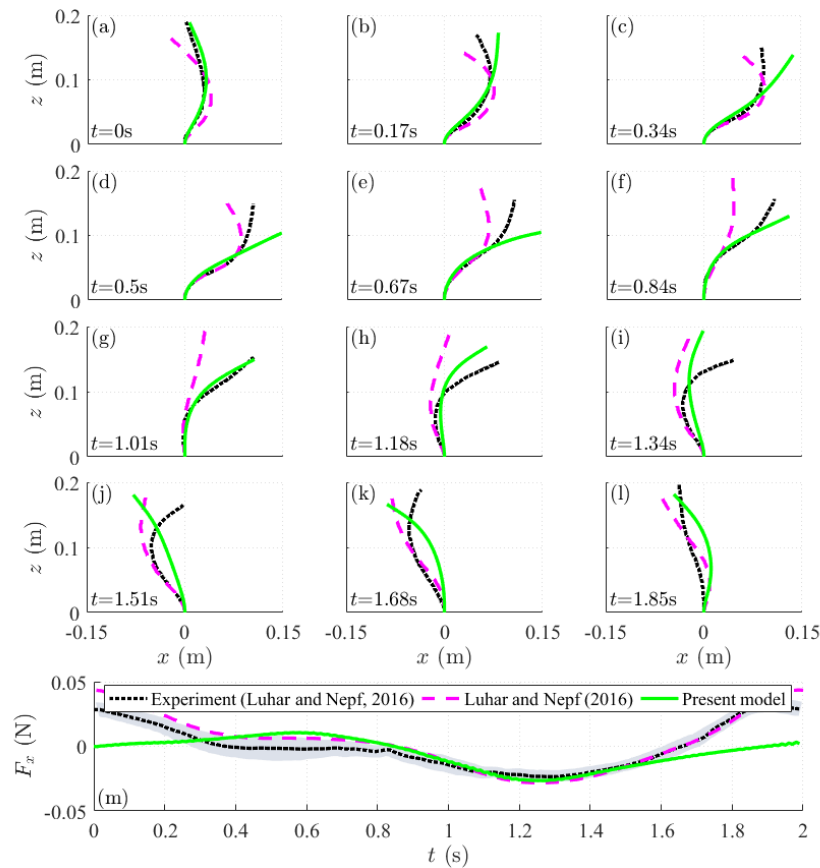
Figure 5. Comparisons for the blade postures and horizontal force over a wave period. (a-l) The observed postures in the experiment are denoted by dotted black lines, the postures predicted by Luhar and Nepf (2016) are denoted by dashed purple lines, and the predictions by present model are denoted by solid green lines. (m) The measured horizontal force at the bottom end of the blade is denoted by black dotted line, the predicted force by Luhar & Nepf (2016) is denoted by purple dashed line, and the prediction by present model is denoted by solid green line. The shaded region represents estimated uncertainty in the experiments by Luhar and Nepf (2016).

The predicted postures of the blade and the total horizontal force were compared with the experimental data and the predictions by Luhar and Nepf (2016), as shown in Figure 5. The predicted blade postures agree with the observed postures for the first half wave period (Fig. 5a-g), except for differences near the blade tip. For the second half of wave period (Fig. 5h-l), the blade postures are underestimated. This is also expressed in the force comparison (Fig. 5m). The predicted force is in good agreement with the data from $t = 0.4$ s to $t = 1.4$ s, but is underestimated for the other wave phases. With a qualitative comparison with the experiments, the coupled model was then used to investigate the wave blade interactions.

RESULTS AND DISCUSSION

The coupled model was used to study the interaction between waves and both bottom-fixed and suspended blades. The simulated wave characteristics and material properties were the same as in Luhar and Nepf (2016). The simulated water depth was 40 cm and the blade length was 10 cm. For the suspended blade case, the top end of the blade was fixed at $z = 0.3$ m and the bottom end was free. The wave-blade interaction was first investigated for the case of a single blade and then followed with canopies.

The most significant process created by the wave-blade interaction was the vortex shedding shown in Fig. 6. The vortex develops at the ends of the blade and sheds following the swaying motion of the blade. Without current, the vortex oscillates following the wave orbital motion. The vortex decays completely when it travels about a quarter wavelength (0.9 m). Therefore, the vortex concentrates near the blade where the vortex was generated. The vortex distribution is asymmetric with the vertical blade in the horizontal direction. More vortices are on the right side of the bottom-fixed blade following the direction of wave propagation while more vortices on the left side of the suspended blade in the opposite direction of the wave propagation. The asymmetric distribution of vortices may be related to the asymmetric swaying motion of the blade, yet this remains to be fully understood.
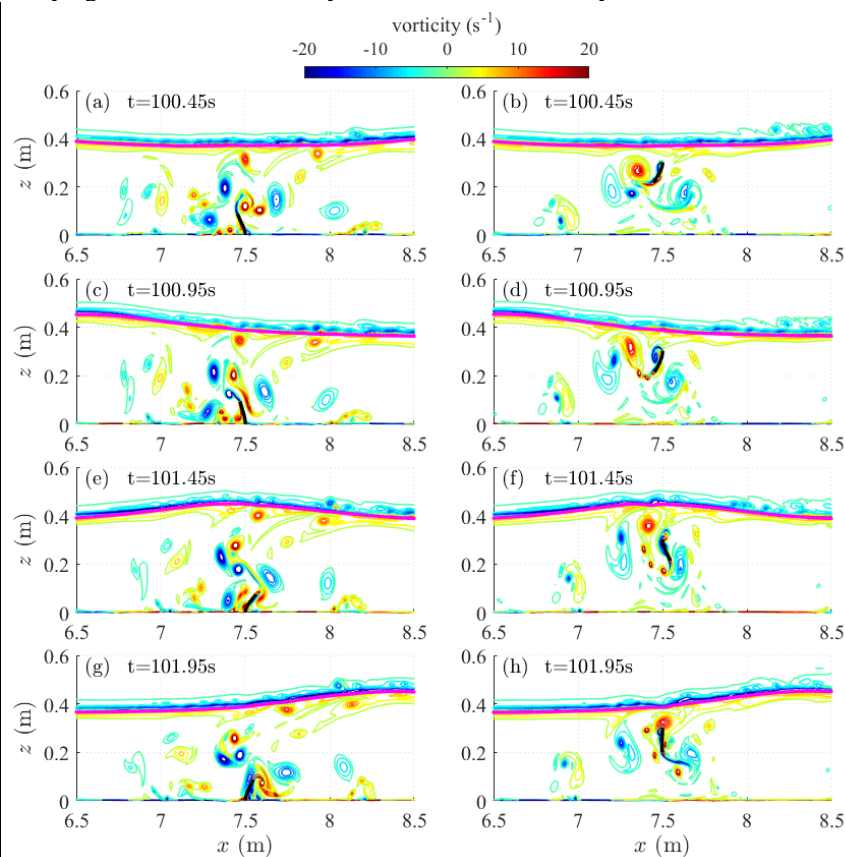
Figure 6. Vorticity contours near a bottom-fixed blade (left column) and a hanging blade (right column) over a wave period. The wave surface is denoted by purple lines near the still water line at $z = 0.4$ m. Four wave phases including wave trough, node (following with crest), crest, node (following with trough) are shown from the top rows to the bottom rows. The blades are denoted by black lines. The positive sign of the vorticity indicates the vortex rotates anticlockwise while the negative sign indicates the ration is clockwise.

The results for the bottom-fixed and suspended canopies are shown in Fig. 7. Similar to a single blade, the vortices develop at the ends of the blades and move following blade motion and wave orbital motion. For the case of a submerged canopy with bottom-fixed blades, the vortices travel upward to the surface. The distribution of the vortices in the horizontal direction is asymmetric with more vortices at the leading edge of the canopy, i.e., in the opposite direction of the wave propagation, which is different from the case of a single blade. For the suspended canopy, the vortices develop at both top and bottom ends. However, the distribution of the vortices is more complicated, with more vortices at the trailing edge of the suspended canopy near the surface above the suspended canopy while more vortices at the leading edge below the bottom of the suspended canopy. One possible reason is the wave and canopy induced currents, which flow in the direction of wave propagation on the top of the bottom-fixed and suspended canopies, while in the opposite direction at the bottom of suspended canopies (Chen et al., 2018). This is consistent with the vorticity distribution for suspended canopies, but not consistent for vortices induced by submerged canopies, where the vortices concentrate at the leading edge while the current flow to downstream. The discrepancy may be caused by the blade swaying motion, which also remains to be fully understood.
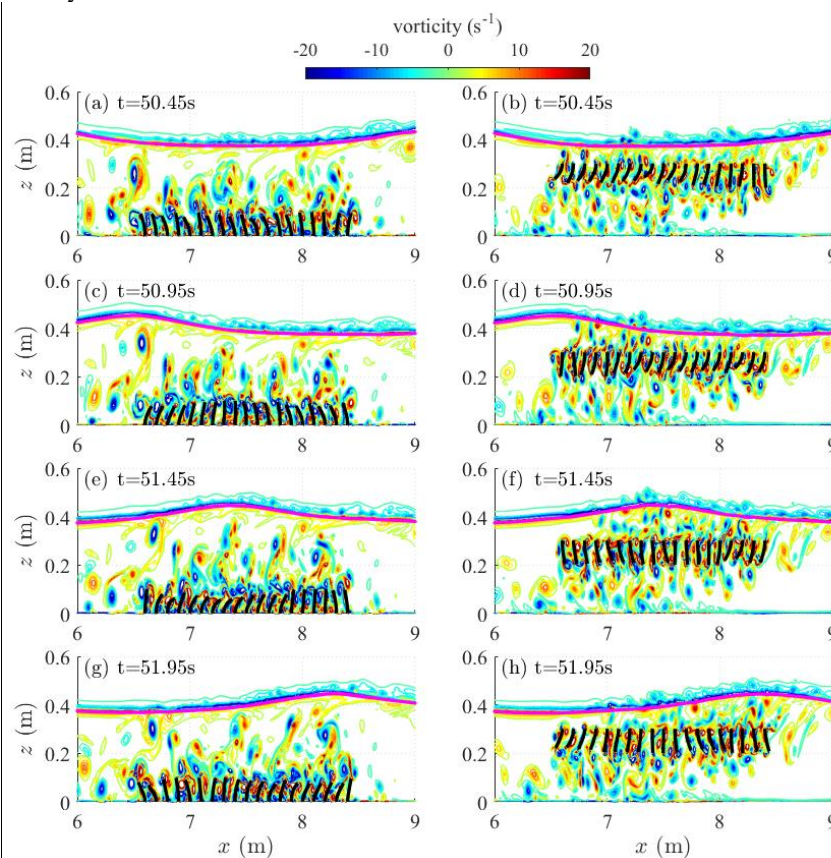
Figure 7. Vorticity contours near a group of bottom-fixed blades (left column) and hanging blades (right column) over a wave period. The wave surface is denoted by purple lines near the still water line at $z = 0.4$ m. Four wave phases including wave trough, node (following with crest), crest, node (following with trough) are shown from the top rows to the bottom rows. The 10 cm-long blades are denoted by black lines.

SUMMARY

In this study, a numerical model was developed to study the interaction between waves and both flexible bottom-fixed and suspended blades as well as submerged and suspended canopies. The dynamics of the blades were simulated by a cable model, which is coupled with OpenFOAM®-based wave model IHFoam with the immersed boundary method. The results showed that the distribution of the blade-induced vortices was asymmetric with more vortices in the wave propagation direction for a single bottom-fixed blade and more vortices in the opposite direction of wave propagation for a single suspended blade. For the case of a submerged canopy, the distribution of vortices was also asymmetric with more vortices were concentrated at the leading edge of the submerged canopy. While for a suspended canopy, more vortices were concentrated at the trailing edge of the suspended canopy near the surface. Near the bottom below the suspended canopy, more vortices were found at the leading edge

of the suspended canopy. The asymmetric distribution of the vortices may influence the nutrient distribution and sediment transport. These results also showed that the effects of blade motion on the vorticity distribution warrant further investigation. The improvement of the coupled model to 3D is desirable.

REFERENCES

Alben, S., Shelley, M., & Zhang, J. 2002. Drag reduction through self-similar bending of a flexible body. *Nature*, 420(6915), 479-481.

Chen, H., Liu, X. and Zou, Q.P., 2018. Wave-driven flow induced by suspended and submerged canopies. *Advances in Water Resources*, 123, 160-172.

Chen, H., Zou, Q. and Liu, Z., 2017. A coupled RANS-VOF and finite element model for wave interaction with highly flexible vegetation. *Proceedings of 35th International Conference on Coastal Engineering*, ASCE, 1(35), 25.

Constant, E., Favier, J., Meldi, M., Meliga, P. and Serre, E., 2017. An immersed boundary method in OpenFOAM: verification and validation. *Computers & Fluids*, 157, pp.55-72.

Higuera, P., Lara, J. L., & Losada, I. J. 2013. Realistic wave generation and active wave absorption for Navier–Stokes models: Application to OpenFOAM®. *Coastal Engineering*, 71, 102-118.

Howell, C. T. 1992. Investigation of the dynamics of low-tension cables. Ph.D. thesis Massachusetts Institute of Technology and Woods Hole Oceanographic Institution.

Luhar, M., Infantes, E., & Nepf, H. 2017. Seagrass blade motion under waves and its impact on wave decay. *Journal of Geophysical Research: Oceans*, 122, 3736–3752.

Luhar, M., & Nepf, H. M. 2016. Wave-induced dynamics of flexible blades. *Journal of Fluids and Structures*, 61, 20-41.

Mullarney, J. C., & Henderson, S. M. 2010. Wave-forced motion of submerged single-stem vegetation. *Journal of Geophysical Research: Oceans* (1978–2012), 115(C12).

Peskin, C. S. 2002. The immersed boundary method. *Acta numerica*, 11, 479-517.

Riahi, H., Meldi, M., Favier, J., Serre, E. and Goncalves, E., 2018. A pressure-corrected Immersed Boundary Method for the numerical simulation of compressible flows. *Journal of Computational Physics*, 374, pp.361-383.

Trianrafyllou, M. S. 1994. Cable mechanics for moored floating structures. *Proceedings of 7th International Conference on the Behaviour of Offshore Structures* (BOSS 1994) (Vol. 2, pp. 57-77).

Zhu, L.-H., & Zou, Q.-P. 2017. Three-layer analytical solution for wave attenuation by suspended and nonsuspended vegetation canopy. *Proceedings of 35th International Conference on Coastal Engineering*, ASCE, 1(35), 27.